fermentation

Article

Synthesis of Tungsten Oxide Nanoflakes and Their Antibacterial and Photocatalytic Properties

Sarinthip Thanakkasaranee [1], Gopinath Kasi [1,*], Sivasamy Kadhiravan [2], Ayyakannu Arumugam [3], Khalid A. Al-Ghanim [4], Mian Nadeem Riaz [5] and Marimuthu Govindarajan [6,7,*]

[1] Division of Packaging Technology, School of Agro-Industry, Faculty of Agro-Industry, Chiang Mai University, Chiang Mai 50100, Thailand
[2] Department of Chemistry, Swami Dayananda College of Arts and Science, Manjakkudi, Tiruvarur 612 610, Affiliated to Bharathidasan University, Tiruchirappalli 620 024, Tamil Nadu, India
[3] Department of Botany, Alagappa University, Karaikudi 630 003, Tamil Nadu, India
[4] Department of Zoology, College of Science, King Saud University, Riyadh 11451, Saudi Arabia
[5] 2476 TAMU, Texas A&M University, College Station, TX 77843, USA
[6] Unit of Mycology and Parasitology, Department of Zoology, Annamalai University, Annamalainagar 608 002, Tamil Nadu, India
[7] Unit of Natural Products and Nanotechnology, Department of Zoology, Government College for Women (Autonomous), Kumbakonam 612 001, Tamil Nadu, India
* Correspondence: gloriousnanogopi@gmail.com (G.K.); drgovind1979@gmail.com (M.G.)

Abstract: This current work revealed a single-step fabrication of tungsten oxide nanoflakes (WO_3 NFs) with the help of *Terminalia arjuna* bark extract. Bioactive phytoconstituents of *T. arjuna* bark extract were involved in the nucleation process and promoted the material crystalline growth in a particular direction. The as-prepared sample thermal decomposition was analyzed by TG/DTG. The as-prepared sample was annealed at 300 °C for 2 h, and the annealed sample was characterized by UV-Vis-DRS, FTIR, Raman, XRD, SEM, EDX, and TEM. Synthesized WO_3 samples showed a monoclinic phase of the flake-like structure with lengths of 25~230 nm and diameters of 25~120 nm. The WO_3 NFs were evaluated against *S. aureus* and *E. coli*. Over 3 mg concentrations of WO_3 NFs outperform the positive control in antibacterial activity. The pseudo-first-order kinetics of the WO_3 NFs enhanced the photocatalytic performance of methylene blue (MB). These results prove that WO_3 NFs have sustainable performance in antibacterial and MB degradation applications.

Keywords: *Terminalia arjuna*; bark extract; nano-flakes; reactive oxygen species; photodegradation

check for updates

Citation: Thanakkasaranee, S.; Kasi, G.; Kadhiravan, S.; Arumugam, A.; Al-Ghanim, K.A.; Riaz, M.N.; Govindarajan, M. Synthesis of Tungsten Oxide Nanoflakes and Their Antibacterial and Photocatalytic Properties. *Fermentation* **2023**, *9*, 54. https://doi.org/10.3390/fermentation9010054

Academic Editor: Nadezhda Sachivkina

Received: 28 October 2022
Revised: 2 January 2023
Accepted: 3 January 2023
Published: 9 January 2023

1. Introduction

Bacterial infections have recently been identified as a major global health threat [1]. For the most part, organic antibiotics have been utilized to treat human bacterial diseases, resulting in bacterial pathogens becoming resistant to antibiotics. However, novel classes of antibiotics slow their further development [2]. On the other hand, the prime source of all living organisms for sustainable development needs is water. The discharges of industrial effluents, especially from the textile industry, such as azo dye, phenyl matter, and toxic organic substances resistant to degradation and decomposition by biological treatment, cause severe water pollution. Chemical markers and biological staining procedures employ methylene blue (MB), a cationic dye. Due to the high chromatic nature and poor biodegradability, it has been complicated to process degradability. More importantly, it causes various harmful effects on human health care, such as diarrhea, vomiting, severe headache, and methemoglobinemia-like syndrome. In addition, it significantly affects the waterbody phytoplankton photosynthesis and microorganism metabolic activity in the water environment [3–6]. Photocatalyst is one of the novel methods to prevent water pollution. Two-dimensional (2D) nanomaterials are efficient catalysts for solving bacterial pathogens, mosquito vectors, and environmental remediation problems. Nowadays, researchers have placed their attention on nanomaterials because they have been used for catalysts' action to produce bio-alcohols due to their reusability. Hitherto, metal and metal oxide Co, Mn, Fe_2O_3, CuO, ZnO, SiO_2, and composites of $CoFe_2O_4@SiO_2$, SrO/SiO_2, CaO-Au, and ZnO–Ag have been used in bioethanol and biobutanol fermentation [7]. Because of their high surface-to-volume ratio, 2D nanostructured materials have recently gained interest for their potential for separation and catalysis. Mainly tungsten oxide (WO_3)-based nanomaterials have been utilized for photocatalysis, sensing, electrochromic devices, paints, dye-sensitized solar cells, CO_2 reduction, batteries, air purification, cancer therapy, and antimicrobial agents [8,9]. They have become more prevalent in recent years because of their inexpensive production costs, configurable bandgap, and great solubility in aqueous solutions under acidic conditions [10]. Typically, WO_3 nanoparticles (NPs) are synthesized by physical and chemical methods such as solvothermal [11], sol-gel [12], reactive magnetron sputtering [10], thermal decomposition [13], acid precipitation [14], hydrothermal synthesis [15], and ion-exchange processes [16]. Supothina et al. [14] reported WO_3 NPs synthesized by the acid precipitation method. The 5.3, 10, and 16 mM concentrations of ammonium tungstate were investigated using 1.5, 3.0, 4.5, and 6.0 pH. In addition, >3 pH concentrations showed a better yield of WO_3. The average size was 30 nm, and the nanoplate dimension was 190 ± 15 nm wide and 50 ± 5 nm thick. The acid precipitation method leads to a 2D nanostructure. However, these physical and chemical methods are expensive; reducing agents and organic solvents are harmful to the environment, high energy, and time-consuming. Therefore, researchers have paid attention to the single-step green synthesis method as an alternative for toxic reducing agents, which is less time-consuming and has large-scale production and ease of handling. Plant-based extracts such as leaves, stems, bark, and roots are rich sources of bioactive reducing compounds and capping agents and can be used for metal and metal oxide NPs or nanomaterial synthesis [17]. The size and shape of nanomaterials from plant extracts vary. According to the literature survey, we chose *Terminalia arjuna* bark extract to prepare WO_3 nanomaterial. It contained phytoconstituents of apigenin, arjun glucoside, arjunic acid, arjunetin, flavonoids, tannins, and triterpenoids [18]. Previously, metal and metal oxide NPs have successfully been synthesized by this plant bark extract [19,20]. We expect that plant bark extract phytoconstituents are helpful in improving the nucleation process leading to different orientations of WO_3 material growth.

Our research focuses on the single-step synthesis of WO_3 nanoflakes (NFs) utilizing *T. arjuna* bark extract. The optical, functional, structural, and topological features of synthesized WO_3 NFs were investigated. Then, they can be used for antibacterial and photocatalytic applications. The synthesized WO_3 NFs had a considerable effect on all activities. To our knowledge, this is the first report on the single-step fabrication of 2D-WO_3 NFs utilizing *T. arjuna* bark extract.

2. Materials and Methods

2.1. Chemical

Himedia, India, provided the nutrient agar and positive control growth media, sterile disk used in this study, whereas Sigma Aldrich supplied the tungstic acid 99%. The experiment was conducted using water that was twice as far apart as normal.

2.2. Plant Material and Microorganism Collection

The *T. arjuna* bark utilized in this research was obtained from Alagappa University Botanical Garden in Karaikudi, Tamil Nadu. The Department Herbarium completed the taxonomical identification of plants with the help of the Flora of the Madras Presidency, India. The Ramakrishna Mission Vivekananda College's Postgraduate and Research Department of Plant Biology and Plant Biotechnology graciously contributed to the bacterium strains (*Staphylococcus aureus* and *Escherichia coli*).

2.3. Plant Bark Extraction Method

Boiling 10 g of *T. arjuna* bark for 10 min in 100 mL of double-distilled water and allowing it cool to 35 °C produced the extract, and it was filtered with Lab world test filter paper 100 dia with 12.5 cm. The obtained solution was used for further experimental uses.

2.4. Synthesis of WO_3 NFs

WO_3 NFs were produced in a typical experiment through a one-step green synthesis process. For this experiment, we used 475 mL of double-distilled water to dissolve 2.5 g of tungstic acid and kept the mixture constantly stirred using a magnetic rod. We added 25 mL of bark extract and stirred it with a magnetic stirrer for 12 h at 80 °C. Subsequently, this yellowish mixture turned into a greenish-yellow color. The continuous stirring pH of the solution was revealed to decrease from 3.5 to 2.5. Parallelly, the non-plant extract method synthesized WO_3 as-prepared sample (reduced the pH 2.5 by diluted HCl). Further, the greenish-yellow precipitate was obtained at two-fourths of the precursor, and this sample was annealed at 300 °C for 2 h in an air atmosphere. Finally, collected WO_3 as-prepared nano-powder was gently grounded by the mortar and pistil. Lastly, we obtained one-half of the sample. Obtained WO_3 nano-powder was stored in a desiccator chamber to avoid the atmosphere's moisture content.

2.5. Characterization of WO_3 NFs

The STA 6000 thermogravimetric analyzer (Perkin Elmer Co., Ltd., Shelton, CT, USA) was used to assess the thermal behavior of the as-prepared sample in a flow of (20 mL/min) N_2 atmosphere; the temperature increased at 5 °C/min from 30 to 725 °C. Samples weighed a total of 21.26 mg. UV-Vis spectroscopy examination was performed on synthetic WO_3 NFs, and a wavelength range of 100 to 1500 nm was recorded using the Shimadzu UV-1600, Tokyo, Japan. Samples of WO_3-NFs were mixed with KBr pellets, and FT–IR spectrophotometers (Bruker Vector 26 spectrometers) were used to identify the functional groups in the sample. RigakuMiniflex X-ray diffractometer (Cu K, 1.5406 A°) was used to analyze the material's crystalline structure from 10° to 90°. The vibrational frequency of the sample was characterized with Bruker-Tensor 27 series spectrophotometer (Bruker Optik GmbH, Ettlingen, Germany) via Raman microscopy (Renishaw, Wotton-under-Edge, UK). We used a Zeiss Field emission scanning electron microscope (FE–SEM) coupled with energy dispersive spectroscopy (EDS) to examine the surface morphology and elemental compositional features. The image was taken at 20 kV voltage and 10 mm working distance. The particle in the sample was dispersed using ultrasonic separation. The WO_3 NFs were studied using a high-resolution transmission electron microscope (HT-TEM), Tecnai G2 20 S-TWIN TEM, with an accelerating voltage of 200 kV. A minute sample was added to 1 mL ethanol for HR-TEM sample preparation and sonicated for 60 min. Then, the solution was drop cast on a carbon-coated Cu-grid.

2.6. Antibacterial Activity

The antibacterial activity of WO_3 NFs was assessed using the agar-disk diffusion technique on *S. aureus* and *E. coli*. Each bacterial strain was cultivated in an aseptic nutrient broth medium for 24 h at 37 °C. It was then carefully poured onto Petri plates to cool. Then, each bacterial suspension was dispersed uniformly across nutrient agar plates. The sterile disk containing 1, 3, 5, and 10 mg WO_3 NFs was then put over the medium using sterile forceps. The positive control was amoxicillin (30 mg). After 24 h of incubation at 37 °C, the inhibition zone diameter produced around the disk was measured. The antibacterial activity was performed as $n = 3$ independent experiments. All results were expressed as means ± standard error (means ± SE).

2.7. Photocatalytic Activity of Methylene Blue

Photodegrading methylene blue (MB) was evaluated for its photocatalytic activity under 300 W Xe lamp illumination. Before, 40 mL L^{-1} MB suspension and 40 mg WO_3 NFs were used. MB absorption–desorption equilibrium was established on the photocatalyst by stirring this solution for 30 min before light illumination. Irradiated samples were taken out every 10 min for extraction and centrifugation for 10 min. A UV-Vis spectrometer measured the MB dye absorption wavelength at 663 nm to determine the dye concentration [20].

3. Results and Discussion

3.1. TG/DTG Measurements of WO_3 NFs

TG is a technique that determines the mass of a sample over time as the temperature varies in a controlled environment. DTG is used to determine a sample's phase transition and thermal behavior. This measurement offers information regarding thermal breakdown absorption, desorption, and kinetic composition analysis. TG/DTG curves of as-synthesized WO_3 as-prepared nano-powder exhibited three thermal decomposition steps. Whereas, over 600 °C, no weight loss was observed in TG, as shown in Figure 1. The first weight loss < 100 °C (2.5%) was assigned to water dehydration for the DTG curve. The second weight loss from 200 to 300 °C (7.5%) was attributed to the decomposition and combustion process of the bio-organic matrix. From 500 to 600 °C (7%), the third step was the related crystallization of tungsten oxide.

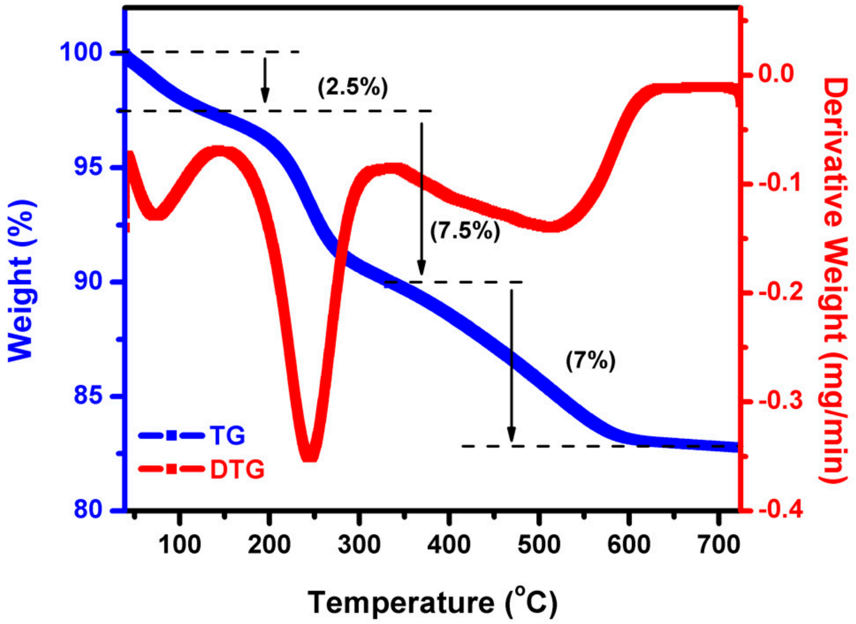

Figure 1. TG/DTG analysis of WO_3 NFs.

3.2. Optical Properties of WO_3 NFs

3.2.1. UV-Vis-DRS Analysis

Figure 2 shows the UV-Vis-diffuse reflectance spectrum of WO_3 NFs. Its n-type W=O bond shifted its absorption to the π-type at 330 nm. For this reason, the Kubelka–Munk equation uses the function equation below [21].

$$\text{Kubelka-Munk equation: } K = (1 - R)2/2R \tag{1}$$

where R = reflectance, F(R) = absorbance. After calculation, the bandgap value was determined to be 2.66 eV. Similarly, Huang et al. reported WO_3 nanorods and revealed a bandgap at 2.48 eV. WO_3 nanorods have a 450 nm absorption peak [22]. Simultaneously, WO_3 nanosheets displayed a red-shifted band edge with 2.75 and 2.38 eV band gaps. The bulk WO_3 bandgap was typically 2.6–3.0 eV. The photogenerated electron-hole pairs on the WO_3 surface lower the bandgap when electrons move from valance to the conduction band [23].

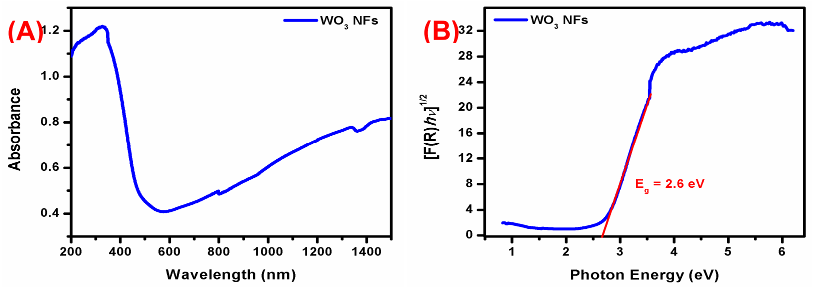

Figure 2. (**A**) UV-Vis-DRS spectrum and (**B**) bandgap analysis of WO_3 NFs.

3.2.2. FT-IR Analysis

Figure 3 shows the FT-IR spectrum of synthesized WO_3 NFs. The band at 3006 cm^{-1} was due to tungsten oxide -OH stretching vibrations [22]. It relates to O-H bending vibrations. Strong bands at 809 and 733 cm^{-1} correspond to W-O-W stretching vibration [24,25]. The wide absorption peak at 1000–500 cm^{-1} was previously thought to be due to stretching vibrations in the WO_3 crystal lattice [26,27]. Earlier studies showed a similar tendency [28]. Non-plant extract synthesized WO_3 spectrum did not show OH stretching and bending vibration. At the same time, the FTIR spectrum of plant bark extracts with various functional group peaks related to the bioactive compounds of *T. arjuna* [18,19]. However, this plant bark-extract functional groups did not appear in the 300 °C 2 h annealing sample. It confirmed the formation of WO_3 material.

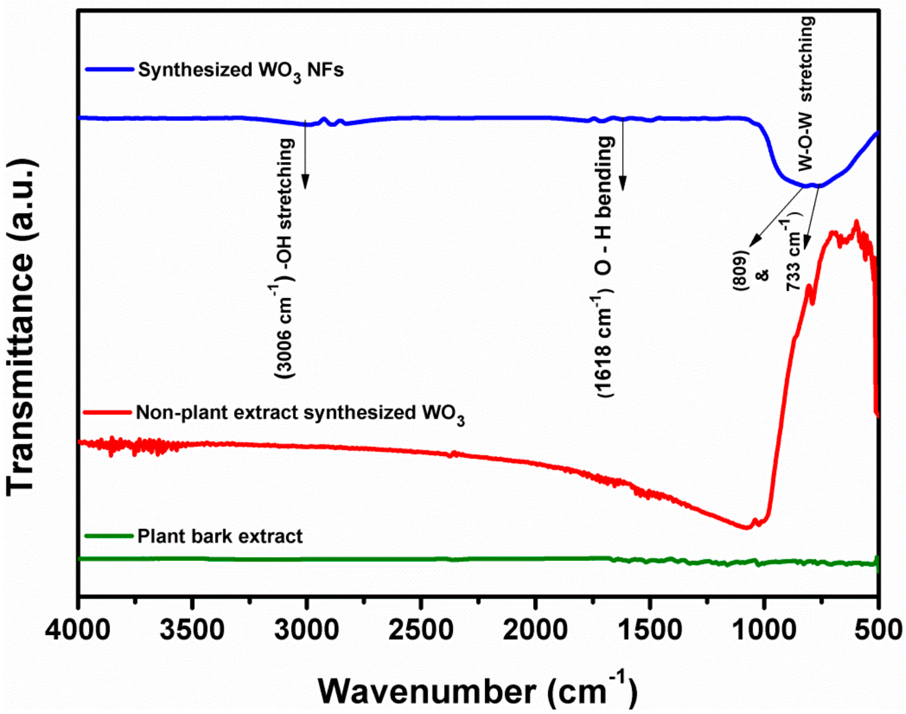

Figure 3. FT-IR analysis of plant extract synthesized WO_3 NFs, non-plant extract synthesized WO_3, and plant bark extract.

3.2.3. Raman Analysis

Figure 4 depicts the intensive Raman bands observed at 71 and 135 cm^{-1} in the low-frequency region, owing to the lattice vibration modes. Similar vibration modes were obtained below at 200 cm^{-1} in the WO_3, which agrees with the previous results [29]. In the Raman spectrum of WO_3 NFs, there were four distinct peaks at 273, 326, 712, and 807 cm^{-1}. The W-O-W bending vibration produced two smaller peaks at 273 and 326 cm^{-1}. Subsequently, the two high-intensity peaks centered at 712 and 807 cm^{-1} are related to

W−O−W stretching vibration [30,31]. Recently, WO_3 NPs produced by *Fusarium solani* revealed two lower-intensity peaks at 267 and 324 cm^{-1} with a flake-like appearance [32].

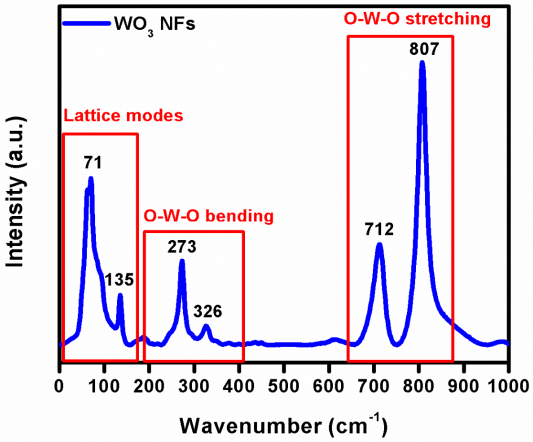

Figure 4. Raman analysis of WO_3 NFs.

3.3. XRD Analysis

The XRD analysis provides phase identification, sample purity, and crystallite size information. Depicted in Figure 5, the XRD patterns of the WO_3 NFs show four main peaks at 2θ = 23.11, 23.58, 24.38, and 34.15° ascribed to indexed with the planes (0 0 2), (0 2 0), (2 0 0), and (2 0 2), respectively. The XRD pattern categorized the monoclinic phase of WO_3 with unit-cell values of a = 7.29 Å, b = 7.53 Å, and c = 7.68 Å, according to JCPDS card no.1314358. The relative four intensities planes (0 0 2), (0 2 0), (2 0 0), and (2 0 2) indicated the highly crystalline nature of the WO_3 phase. Parthibavarman et al. reported that WO_3 nanorods and nanosheets showed (0 0 2), (0 2 0), and (2 0 0) planes leading to a high crystalline nature [33]. However, the intensity of the (0 0 2) plane was increased for WO_3 nanorods compared to WO_3 nanosheets. Our result was consistent with the aforementioned WO_3 nanosheet's crystalline nature [33].

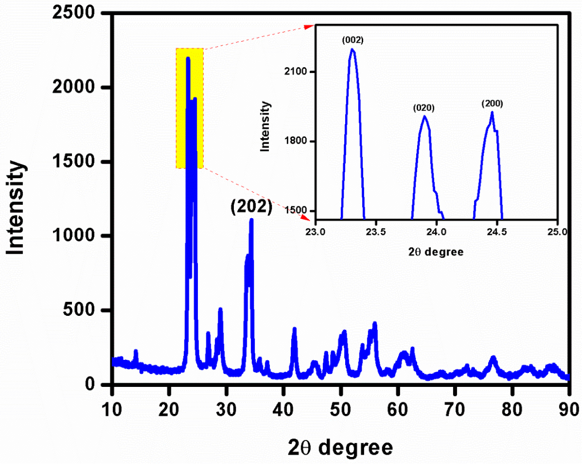

Figure 5. XRD analysis of WO_3 NFs.

3.4. FE-SEM with EDX Analysis

FE-SEM analysis provides a surface topology that leads to two-dimensional images with high resolution. As shown in Figure 6, this synthesized method obtained the flake-like morphology of WO_3 NFs. Furthermore, the elemental composition, weight, and atomic percentage are classified by the EDX spectral analysis. The EDX profile of WO_3 NFs showed W and O elements and did not find any more impurity peaks. The atomic weight percentage of W and O was 25 and 75%, respectively, which confirmed the formation of WO_3 NFs of purity.

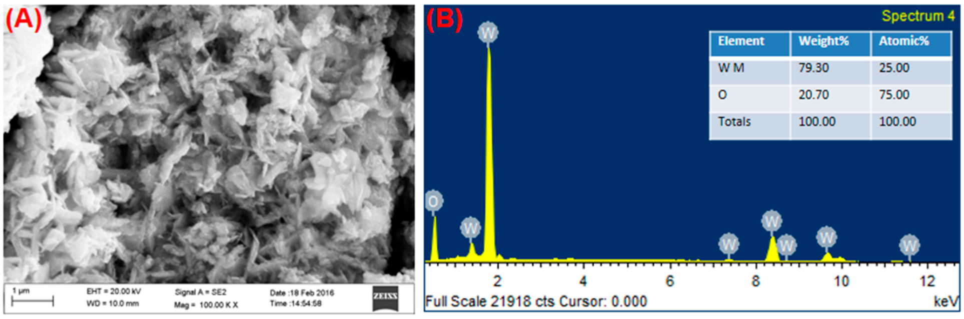

Element	Weight%	Atomic%
W M	79.30	25.00
O	20.70	75.00
Totals	100.00	100.00

Figure 6. (**A**) SEM and (**B**) EDX analysis of WO_3 NFs.

3.5. HR-TEM Analysis of WO_3 NFs

The accurate particle size, shape, and crystalline behavior of WO_3 NFs were confirmed by HR-TEM images and SAED. Figure 7 shows the flake-like structure with lengths of 25~230 nm and diameters of 25~120 nm. The interplanar spacing was 0.373 nm, related to the (020) planes of monoclinic WO_3 NFs. An HR-TEM result of synthesized WO_3 NFs clearly showed that the growth direction is along the (020) plane. On the HR-TEM picture of WO_3 NFs SAED patterns highlighted the NF's crystalline structure.

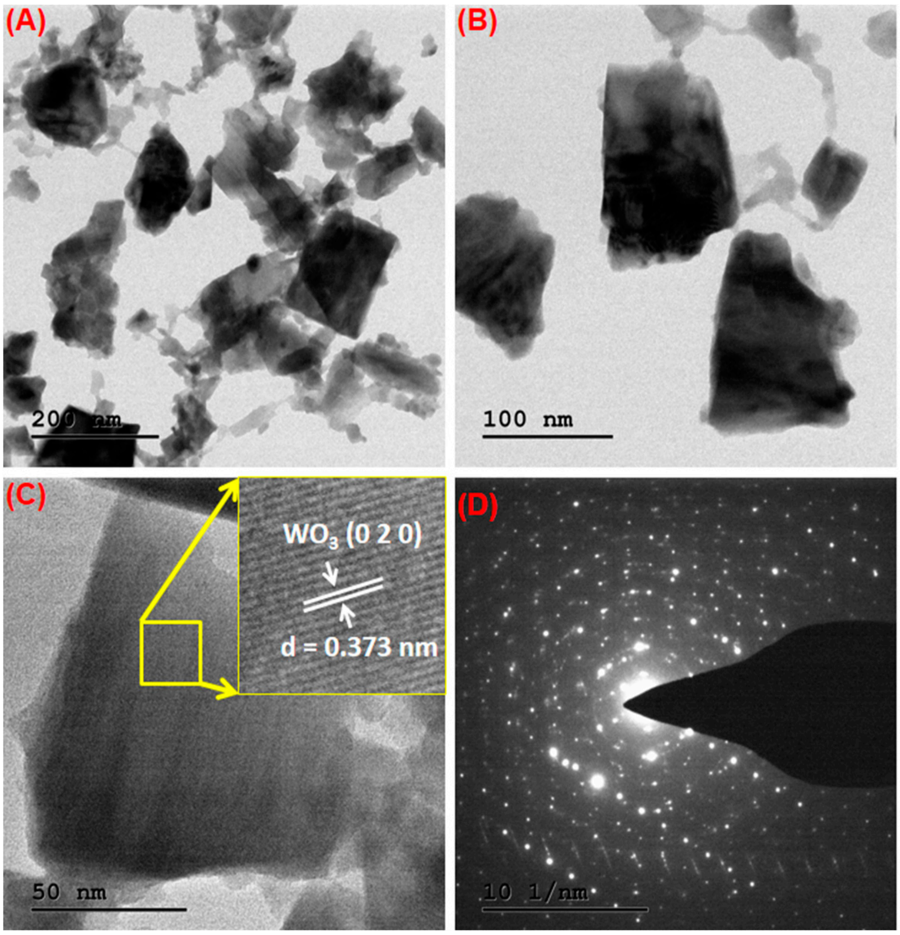

Figure 7. (**A**–**C**) TEM images, (**D**) SAED patterns of WO_3 NFs.

3.6. Antibacterial Activity of WO_3 NFs

The size, shape, aspect ratio, surface charge, stability, and surface defect of nanoparticles were all shown to be important factors in their antibacterial activity [34]. The current study shows the antibacterial activity of WO_3 NFs, as shown in Figures 8 and 9. The *E. coli* bacterial strain showed a maximum zone of inhibition compared to the *S. aureus* at 10 mg concentration, related to the bacterial cell wall structure. The antibacterial activity results exhibited are dependent on increasing the content of WO_3 NFs. The WO_3 NFs contact the bacterial cell wall by electrostatic attraction. This is followed by ROS produced by the bacterial cell wall: superoxide-anions ($O_2\bullet^-$), hydroxyl radicals ($\bullet$OH), hydrogen peroxides (H_2O_2), and singlet oxygen (${}_1O^2$). This ROS generation leads to inhibits bacterial survivability. It caused the malfunction of intracellular organelles, interference of cell signaling, collapses in DNA replication, protein and ATP synthesis, imbalance in the electron transfer system, and enzyme kinetics. These factors inhibited bacterial growth and caused the loss of cytoplasmic electrolyte fluids, which led to cell death, as shown in Figure 10. The WO_3 NFs induced ROS generation as follows.

$$WO_3 + h\nu \rightarrow e^- + h^+$$

$$h^+ + H_2O \rightarrow {}^\bullet OH + H^-$$

$$e^- + O_2 \rightarrow {}^\bullet O_2{}^-$$

$${}^\bullet O_2{}^- + H^+ \rightarrow HO_2\bullet$$

$$HO_2\bullet + H^+ + e^- \rightarrow H_2O_2$$

Both *E. coli* and *S. aureus* may be killed by the WO_3-X nanodots in a dose and time-dependent way to better rupture the bacterial membranes [35]. WO_3 and rGO-WO_3 (100 g/mL) composite sheets in 2D rectangular shapes inhibited the development of bacteria and severely damaged the cell wall of *B. subtilis*, according to Ahmed et al. [36]. This study suggested that WO_3 NFs influence the control of bacterial growth, especially against Gram-negative bacteria.

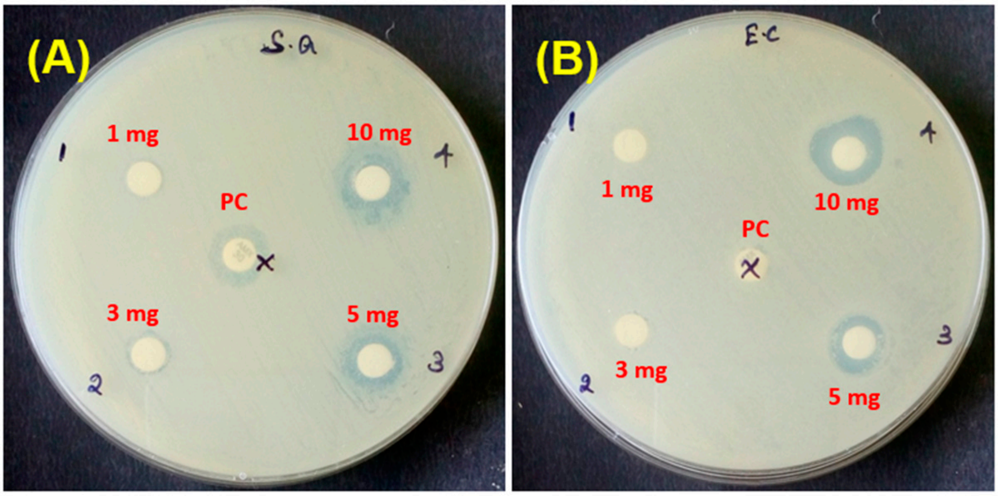

Figure 8. Antibacterial activity of WO_3 NFs; (**A**) *S. aureus* and (**B**) *E. coli*.

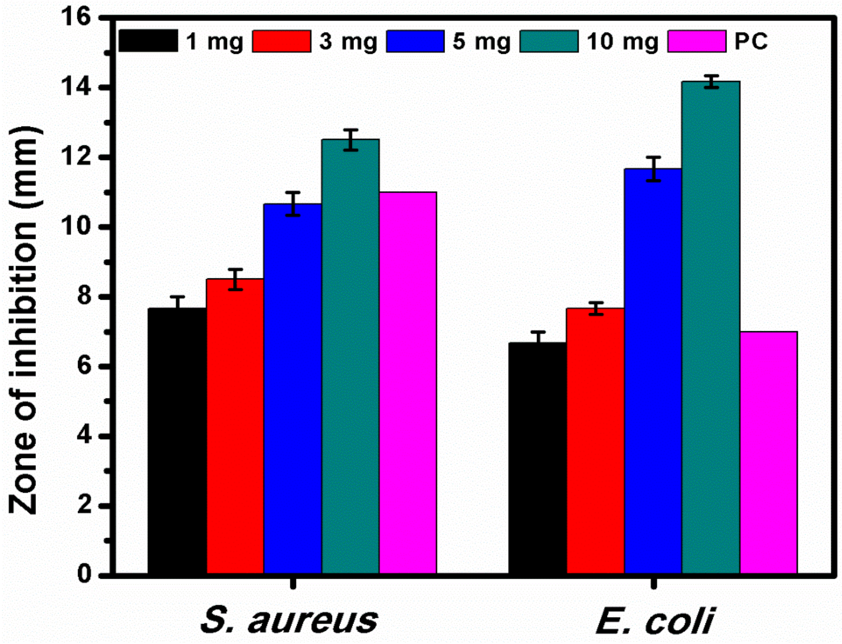

Figure 9. Different concentrations of WO_3 NFs tested against *S. aureus* and *E. coli*. PC, positive control (Amoxicillin—30 mg).

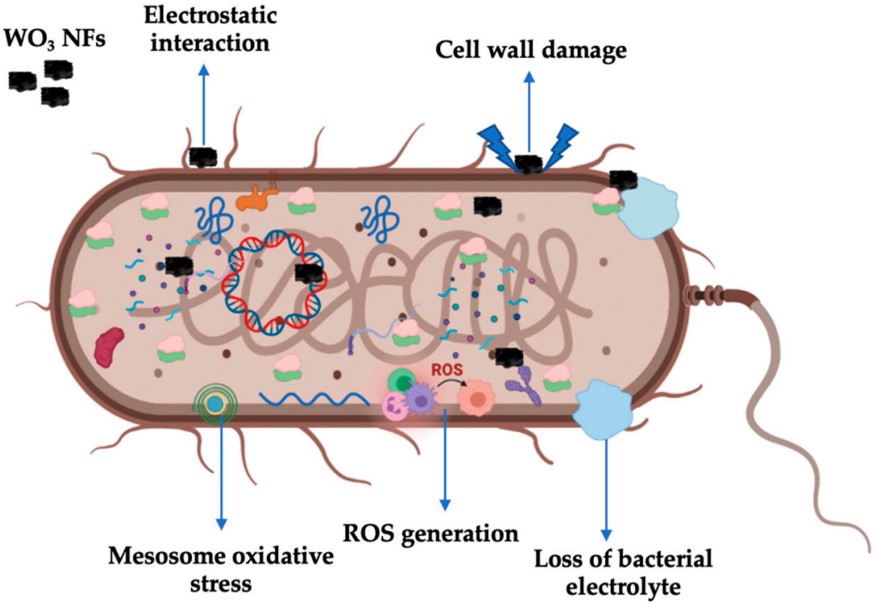

Figure 10. Antibacterial mechanism of WO_3 NFs.

3.7. Methylene Blue Photocatalytic Degradation

Under visible light irradiation, the photocatalytic performance of WO_3 NFs towards the decolorization of MB dye was investigated. Figure 11A shows the variation of MB concentration (*C/C0*) at time intervals. The WO_3 NFs exhibit higher photocatalytic performance compared to the plant extract treatment of MB (Figure 11C). Almost 85.7% of MB was degraded within 40 min using WO_3 NFs, as shown in Figure 11B,D. Due to the increased charge separation between photogenerated electron and hole pairs, significant improvements in photodegradation were seen. Photodegradation of MB dyes using pseudo-first-order kinetic model ln (*C0/C*) = Kt value is for WO_3 NFs.

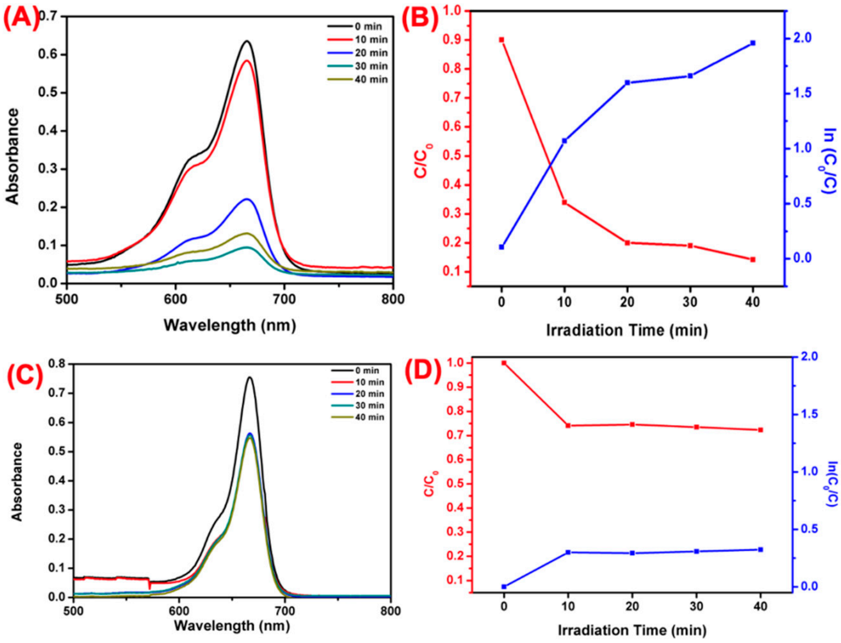

Figure 11. Visible-light-induced photodegradation of MB. (**A**) Different time irradiation WO_3 NFs, (**B**) plotted against; (*C/C0*) and ln(*C0/C*). (**C**) Different time irradiation plant bark extract, (**D**) plotted against (*C/C0*) and ln(*C0/C*).

4. Conclusions

We successfully synthesized WO_3 NFs using *T. arjuna* bark extract by a one-step method and evaluated the antibacterial activity and photocatalytic degradation with MB dye. Optical band gap values showed at 2.6 eV, and the FTIR functional groups revealed the formation of WO_3 by forming two high-intensity peaks centered at 712 and 807 cm^{-1}. The XRD results exhibit high crystalline nature with a monoclinic phase. The topological analysis of SEM and TEM analysis showed a flake-like structure. The antibacterial activity of WO_3 NFs excellently inhibited *E. coli* at the 10 mg concentration compared to *S. aureus* due to the Gram-negative bacteria's thin cell wall structural configuration. Overall, antibacterial activity illustrates a dose-dependent effect. At the same time, ROS generation of H_2O_2 causes DNA damage, protein denaturation, and cytoplasmic electrolyte leakage leading to bacterial lysis. In addition, MB photodegradation of WO_3 NFs showed an efficiency of 85.7%. This process was easy, fast, inexpensive, sustainable, and scalable. Conveniently, the one-step green route alternates between physical and chemical methods. Synthesized WO_3 NFs can be used for antibacterial and photocatalytic applications. As a result, this material may be used in various disciplines, including energy storage and biological applications.

Author Contributions: Conceptualization, S.T., G.K., M.G.; methodology, S.T., G.K.; software, M.G.; validation, S.T., G.K., M.G., A.A., S.K., K.A.A.-G.; formal analysis, A.A., S.T., G.K.; resources, M.G., K.A.A.-G.; visualization, M.N.R.; writing—original draft preparation, S.T., G.K.; writing—review and editing, M.G., M.N.R.; funding acquisition, K.A.A.-G. All authors have read and agreed to the published version of the manuscript.

Funding: Researchers Supporting Project Number (RSP2023R48) King Saud University, Riyadh, Saudi Arabia. This research was supported by the Post-Doctoral Fellowship Reinventing University program fund of Chiang Mai University, Chiang Mai, Contract number: 10/2022. This research work was also partially supported by Chiang Mai University.

Institutional Review Board Statement: Not applicable.

Informed Consent Statement: Not applicable.

Data Availability Statement: The datasets analyzed during the current study are available from the corresponding author upon reasonable request.

Acknowledgments: The authors express their sincere appreciation to the Researchers Supporting Project Number (RSP2023R48), King Saud University, Riyadh, Saudi Arabia.

Conflicts of Interest: These authors declare no competing financial interest.

References

1. Zou, Z.; Sun, J.; Li, Q.; Pu, Y.; Liu, J.; Sun, R.; Wang, L.; Jiang, T. Vancomycin modified copper sulfide nanoparticles for photokilling of vancomycin-resistant enterococci bacteria. *Colloids Surf. B Biointerfaces* **2020**, *189*, 110875. [CrossRef] [PubMed]
2. Wang, W.; Cheng, X.; Liao, J.; Lin, Z.; Chen, L.; Liu, D.; Zhang, T.; Li, L.; Lu, Y.; Xia, H. Synergistic photothermal and photodynamic therapy for effective implant-related bacterial infection elimination and biofilm disruption using Cu9S8 nanoparticles. *ACS Biomater. Sci. Eng.* **2019**, *5*, 6243–6253. [CrossRef] [PubMed]
3. Rai, H. Removal of dyes from textile manufacturing effluent of textile and dyestuff manufacturing industry: A review of emerging techniques with reference to biological treatment. *Crit. Rev. Environ. Sci. Technol.* **2005**, *35*, 219–238. [CrossRef]
4. Shokoohi, R.; Nematollahi, D.; Samarghandi, M.R.; Azarian, G.; Latifi, Z. Optimization of three-dimensional electrochemical process for degradation of methylene blue from aqueous environments using central composite design. *Environ. Technol. Innov.* **2020**, *18*, 100711. [CrossRef]
5. Indana, M.K.; Gangapuram, B.R.; Dadigala, R.; Bandi, R.; Guttena, V. A novel green synthesis and characterization of silver nanoparticles using gum tragacanth and evaluation of their potential catalytic reduction activities with methylene blue and Congo red dyes. *J. Anal. Sci. Technol.* **2016**, *7*, 19. [CrossRef]
6. Kuang, Y.; Zhang, X.; Zhou, S. Adsorption of methylene blue in water onto activated carbon by surfactant modification. *Water* **2020**, *12*, 587. [CrossRef]
7. Kushwaha, D.; Upadhyay, S.; Mishra, P. Nanotechnology in bioethanol/biobutanol production. In *Green Nanotechnology for Biofuel Production*; Springer: Berlin/Heidelberg, Germany, 2018; pp. 115–127.
8. Moudgil, A.; Dhyani, V.; Das, S. High speed efficient ultraviolet photodetector based on 500 nm width multiple WO_3 nanowires. *Appl. Phys. Lett.* **2018**, *113*, 101101. [CrossRef]
9. Mardare, C.C.; Hassel, A.W. Review on the versatility of tungsten oxide coatings. *Phys. Status Solidi* **2019**, *216*, 1900047. [CrossRef]
10. Verma, M.; Singh, K.P.; Kumar, A. Reactive magnetron sputtering based synthesis of WO_3 nanoparticles and their use for the photocatalytic degradation of dyes. *Solid State Sci.* **2020**, *99*, 105847. [CrossRef]
11. Jeevitha, G.; Mangalaraj, D. Ammonia sensing at ambient temperature using tungsten oxide (WO_3) nanoparticles. *Mater. Today Proc.* **2019**, *18*, 1602–1609. [CrossRef]
12. Susanti, D.; Diputra, A.G.P.; Tananta, L.; Purwaningsih, H.; Kusuma, G.E.; Wang, C.; Shih, S.; Huang, Y. WO_3 nanomaterials synthesized via a sol-gel method and calcination for use as a CO gas sensor. *Front. Chem. Sci. Eng.* **2014**, *8*, 179–187. [CrossRef]
13. Yan, H.; Zhang, X.; Zhou, S.; Xie, X.; Luo, Y.; Yu, Y. L232- Synthesis of WO_3 nanoparticles for photocatalytic O_2 evolution by thermal decomposition of ammonium tungstate loading on g-C_3N_4. *J. Alloys Compd.* **2011**, *509*, L235. [CrossRef]
14. Supothina, S.; Seeharaj, P.; Yoriya, S.; Sriyudthsak, M. Synthesis of tungsten oxide nanoparticles by acid precipitation method. *Ceram. Int.* **2007**, *33*, 931–936. [CrossRef]
15. Ahmadi, M.; Younesi, R.; Guinel, M.J.-F. Synthesis of tungsten oxide nanoparticles using a hydrothermal method at ambient pressure. *J. Mater. Res.* **2014**, *29*, 1424–1430. [CrossRef]
16. Lu, Z.; Kanan, S.M.; Tripp, C.P. Synthesis of high surface area monoclinic WO_3 particles using organic ligands and emulsion based methods. *J. Mater. Chem.* **2002**, *12*, 983–989. [CrossRef]
17. Alharbi, N.S.; Govindarajan, M.; Kadaikunnan, S.; Khaled, J.M.; Almanaa, T.N.; Alyahya, S.A.; Al-Anbr, M.N.; Gopinath, K.; Sudha, A. Nanosilver crystals capped with Bauhinia acuminata phytochemicals as new antimicrobials and mosquito larvicides. *J. Trace Elem. Med. Biol.* **2018**, *50*, 146–153. [CrossRef]
18. Gopinath, K.; Kumaraguru, S.; Bhakyaraj, K.; Thirumal, S.; Arumugam, A. Eco-friendly synthesis of TiO_2, Au and Pt doped TiO_2 nanoparticles for dye sensitized solar cell applications and evaluation of toxicity. *Superlattices Microstruct.* **2016**, *92*, 100–110. [CrossRef]
19. Gopinath, K.; Sundaravadivelan, C.; Arumugam, A. Green synthesis, characterization of silver, gold and bimetallic nanoparticles using bark extract of Terminalia arjuna and their larvicidal activity against malaria vector, Anopheles stephensi. *Int. J. Recent Sci. Res.* **2013**, *4*, 904–910.
20. Mahboob, S.; Nivetha, R.; Gopinath, K.; Balalakshmi, C.; Al-Ghanim, K.A.; Al-Misned, F.; Ahmed, Z.; Govindarajan, M. Facile synthesis of gold and platinum doped titanium oxide nanoparticles for antibacterial and photocatalytic activity: A photodynamic approach. *Photodiagnosis Photodyn. Ther.* **2021**, *33*, 102148. [CrossRef]
21. Choudhury, B.; Dey, M.; Choudhury, A. Defect generation, dd transition, and band gap reduction in Cu-doped TiO_2 nanoparticles. *Int. Nano Lett.* **2013**, *3*, 25. [CrossRef]
22. Huang, D.; Zheng, C.; Huang, L.; Wu, X.; Chen, L. Linear and nonlinear optical properties of ultrafine WO_3 nanorods. *Optik* **2018**, *156*, 994–998. [CrossRef]
23. Huang, L.; Xu, H.; Li, Y.; Li, H.; Cheng, X.; Xia, J.; Xu, Y.; Cai, G. Visible-light-induced WO_3/gC_3N_4 composites with enhanced photocatalytic activity. *Dalton Trans.* **2013**, *42*, 8606–8616. [CrossRef] [PubMed]

24. Mane, A.; Navale, S.; Sen, S.; Aswal, D.; Gupta, S.; Patil, V. Nitrogen dioxide (NO_2) sensing performance of p-polypyrrole/n-tungsten oxide hybrid nanocomposites at room temperature. *Org. Electron.* **2015**, *16*, 195–204. [CrossRef]
25. Li, S.; Lin, P.; Zhao, L.; Wang, C.; Liu, D.; Liu, F.; Sun, P.; Liang, X.; Liu, F.; Yan, X. The room temperature gas sensor based on Polyaniline@flower-like WO_3 nanocomposites and flexible PET substrate for NH3 detection. *Sens. Actuators B Chem.* **2018**, *259*, 505–513. [CrossRef]
26. Bai, S.; Zhang, K.; Wang, L.; Sun, J.; Luo, R.; Li, D.; Chen, A. Synthesis mechanism and gas-sensing application of nanosheet-assembled tungsten oxide microspheres. *J. Mater. Chem. A* **2014**, *2*, 7927–7934. [CrossRef]
27. Liu, F.; Chen, X.; Xia, Q.; Tian, L.; Chen, X. Ultrathin tungsten oxide nanowires: Oleylamine assisted nonhydrolytic growth, oxygen vacancies and good photocatalytic properties. *RSC Adv.* **2015**, *5*, 77423–77428. [CrossRef]
28. Badilescu, S.; Ashrit, P. Study of sol–gel prepared nanostructured WO_3 thin films and composites for electrochromic applications. *Solid State Ion.* **2003**, *158*, 187–197. [CrossRef]
29. De Wijs, G.; De Groot, R. Amorphous WO_3: A first-principles approach. *Electrochim. Acta* **2001**, *46*, 1989–1993. [CrossRef]
30. Xu, L.; Yin, M.-L. Ag_x@WO_3 core-shell nanostructure for LSP enhanced chemical sensors. *Sci. Rep.* **2014**, *4*, 6745. [CrossRef]
31. Boruah, P.J.; Khanikar, R.R.; Bailung, H. Synthesis and characterization of oxygen vacancy induced narrow bandgap tungsten oxide (WO_{3-x}) nanoparticles by plasma discharge in liquid and its photocatalytic activity. *Plasma Chem. Plasma Process.* **2020**, *40*, 1019–1036. [CrossRef]
32. Kavitha, N.; Venkatesh, K.; Palani, N.; Ilangovan, R. Fungus mediated biosynthesis of WO_3 nanoparticles using Fusarium solani extract. *Proc. AIP Conf. Proc.* **2017**, *1832*, 050130.
33. Parthibavarman, M.; Karthik, M.; Prabhakaran, S. Facile and one step synthesis of WO_3 nanorods and nanosheets as an efficient photocatalyst and humidity sensing material. *Vacuum* **2018**, *155*, 224–232. [CrossRef]
34. Kasi, G.; Viswanathan, K.; Sadeghi, K.; Seo, J. Optical, thermal, and structural properties of polyurethane in Mg-doped zinc oxide nanoparticles for antibacterial activity. *Prog. Org. Coat.* **2019**, *133*, 309–315. [CrossRef]
35. Duan, G.; Chen, L.; Jing, Z.; De Luna, P.; Wen, L.; Zhang, L.; Zhao, L.; Xu, J.; Li, Z.; Yang, Z. Robust antibacterial activity of tungsten oxide (WO_{3-X}) nanodots. *Chem. Res. Toxicol.* **2019**, *32*, 1357–1366. [CrossRef] [PubMed]
36. Ahmed, B.; Ojha, A.K.; Singh, A.; Hirsch, F.; Fischer, I.; Patrice, D.; Materny, A. Well-controlled in-situ growth of 2D WO_3 rectangular sheets on reduced graphene oxide with strong photocatalytic and antibacterial properties. *J. Hazard. Mater.* **2018**, *347*, 266–278. [CrossRef]